Supporting Information

The Impact of Alkoxy Side Chains on the Solubility, Thermoelectric, and Photothermal Performance of Metal Coordination Polymers

*Wenwen You, Run Kang, Nuo Xu, Fei Jiao**

General Experimental

All chemicals were purchased from Sigma-Aldrich and were used without further purification. Reactions were carried out under nitrogen atmosphere using standard Schlenk techniques and reported yields refer to purified and spectroscopically pure compounds, unless otherwise stated.

^{1}H and ^{13}C nuclear magnetic resonance (NMR) spectra were recorded on Bruker NMR spectrometers Avance III 400 and Avance Neo 700 at 298 K. Chemical shifts (δ) are reported in parts per million (ppm), using the residual solvent peaks as internal standard. For ^{1}H-NMR (δ): $CDCl_3$ 7.26. For ^{13}C-NMR (δ): $CDCl_3$ 77.16. Coupling constants (J) are given in Hertz (Hz) and spin multiplicities are denoted as follows: s = singlet, d = doublet, hept = heptet.

The Scanning Electron Microscope (SEM) images were obtained by a Hitachi Regulus8100 SEM. The energy dispersive X-ray spectroscope (EDS, Oxford) fitted to the SEM was utilized in mapping mode for elemental analysis.

The Powder X-ray Diffraction (PXRD) data were collected by using Aries (Panalytical) equipped with Cu Kα radiation (λ = 1.5404 Å). The samples were measured by Bragg-Brentano reflection mode with the Bragg angle (2θ) ranging from 5° to 40° and a step size of 0.03° at 1 s per step. Before diffraction testing, the crystals have been well grounded to eliminate orientation.

The quantitative elemental analysis was performed by the combination of CHN elemental analysis (Flash EA 1112, Thermo Fisher Scientific) and inductively coupled plasma-optical emission spectroscopy (ICP-OES, iCAP 6300 Radial, Thermo Scientific).

Carbon content analysis has been performed by elemental analysis. Nickel contents have been measured by using inductively coupled plasma optical emission spectrometry. For ICP-OES measurements, the samples were prepared by dissolving them in fuming nitric acid and diluted to a known volume with Milli-Q water.

Thermogravimetric analysis (TGA) was performed on a TA Instruments Q500 Thermogravimetric Analyzer at a heating rate of 2.0 °C min^{-1} under air or N_2 gas flow of 5 mL min^{-1} on a platinum pan from room temperature to 800 °C.

The X-ray photoelectron spectroscopy (XPS) and ultraviolet photoelectron spectroscopy (UPS) characterization were performed on a Kratos AXIS Ultra DLD ultrahigh vacuum photoelectron spectroscopy system using a monochromatic Al Kα X-ray (1486.6 eV) and a He-discharge lamp (He *I*, 21.22 eV) as the excitation sources, respectively. For UPS measurements, the samples were negatively biased at 5.0 V to enable observation of secondary electron cut-off. The Fermi edge was calibrated from a UPS spectrum of Ar ion sputtered clean Au substrate and was defined as the zero binding energy.

Electron paramagnetic resonance spectroscopy (EPR) measurements were performed under nitrogen in septum-sealed quartz tubes using a Bruker EMX spectrometer equipped with an ER 4199HS cavity and Gunn diode microwave source at ~5 K, with a microwave frequency of 9.37 GHz, power of 0.100 mW, and attenuation of 33.0 dB. The measurements were taken in perpendicular mode. Pure powder samples were used for the measurements.

Fourier-transform infrared spectra were obtained as KBr pellets using a Bruker Vertex 70 spectrometer, covering the range of 400 to 4000 cm^{-1}. Data were processed and background corrected with the OPUS software (version 7.5). An additional manual correction for scattering was also applied.

Raman spectra were recorded using a Horiba LabRAM HR Evolution Raman microscope in the range of 200-4000 cm^{-1} at 298 K. The spectral resolution was 4 cm^{-1}, and 256 scans were accumulated for each measurement.

The Ni K-edge X-ray absorption near-edge structure (XANES) and extended X-ray absorption fine structure (EXAFS) spectra were collected at MRCAT 10-BM beamline. Data collection was carried out in transmission mode using ionization chamber for Ni foil, using a Lytle detector for sample-Ru and sample-Ir. All spectra were collected in ambient

conditions. The data were processed according to standard procedures using the Athena module implemented in the IFEFFIT software packages. The EXAFS spectra were obtained by subtracting the post-edge background from the overall absorption and then normalizing with respect to the edge-jump step. Subsequently, the $\chi(k)$ data were Fourier transformed to real (R) space using a hanning windows (dk = 1.0 Å^{-1}) to separate the EXAFS contributions from different coordination shells. To obtain the quantitative structural parameters around central atoms, least-squares curve parameter fitting was performed using the ARTEMIS module of IFEFFIT software packages.[1,2]

A PerkinElmer Lambda 750 UV-vis-NIR absorption spectrometer was used to conduct spectral analysis in the spectrum range of 200-2500 nm. The scanning speed was maintained at 600 nm min^{-1} in the experiment, and the tests were all completed at room temperature.

The specific heat C_p was measured using a differential scanning calorimeter (DSC, STA 449F3) with a sapphire standard reference method. High-purity synthetic sapphire (α-Al_2O_3, 25.13 mg) and the sample were loaded into identical aluminum crucibles and subjected to identical thermal profiles under a 100 mL min^{-1} N_2 atmosphere. The temperature was ramped from 20 °C to 80 °C at a rate of 10 °C min^{-1}. The C_p of Ni-BTT-OCn was calculated using:

$$C_{\mathrm{p\ sample}} = \frac{\Phi_{\mathrm{sample}}}{\Phi_{\mathrm{sapphire}}} \frac{m_{\mathrm{sapphire}}}{m_{\mathrm{sample}}} C_{\mathrm{p\ sapphire}}$$

where m_{sample} and m_{sapphire} denote the mass of the sample and sapphire, respectively. Φ_{sample} and Φ_{sapphire} denote the heat flux signals of the sample and sapphire, respectively. $C_{\mathrm{p\ sapphire}}$ represents the specific heat capacity of sapphire. Baseline corrections were applied to eliminate instrumental drift. Each measurement was repeated three times to ensure reproducibility.

Ni-BTT-OCn samples were pressed into pellet samples under 10 MPa of pressure by using a rectangular mold. The size of the pellet sample is 2 mm × 5 mm which was determined by the mold size. The thickness of the pellet sample depends on the weight of Ni-BTT-OCn used. For example, for a 30 mg pellet, the thickness is about 1.5 mm. Four parallel gold electrodes were deposited onto a square quartz glass sheet (10 mm × 10 mm × 0.5 mm) using a mask plate, ensuring a distance of 1 mm between adjacent electrodes.

Each electrode was coated with an appropriate amount of conductive silver paste, and the pressed pellet was adhesively bonded to the glass substrate containing the four gold electrodes to establish a conductive pathway. The device was then placed in a sealed sample chamber and measured under high vacuum conditions in a dark environment utilizing a TETF-LN thin film thermoelectric parameter tester. A power module supplied a constant current, while a high-precision voltmeter was employed to measure the voltage across both ends of the device. The conductivity can be calculated using the formula:

$$\sigma = \frac{L}{RS}$$

where R represents the resistance of the device, L is its length, and S denotes its cross-sectional area.

To further explore the conduction mechanism, three-dimensional Mott variable-range hopping (3D VRH) models were examined, the conductivity of which, σ_{VRH}, is described by:

$$\sigma_{\mathrm{VRH}} = \sigma_0 \exp\left[-\left(\frac{T_0}{T}\right)^x\right]$$

where σ_0 is a conductivity prefactor and T_0 is a characteristic temperature with an exponent x. In our case, we applied a Mott 3D hopping model (x = 1/4).

In a Mott model, T_0 is related to $D(E_{\mathrm{F}})$ by a relation of form:

$$T_0 = \frac{a}{k_{\mathrm{B}} D(E_{\mathrm{F}}) \xi^3}$$

where a is a theoretical scaling constant (64 based on numerical calculations); ξ is the decay length or localization length; $D(E_{\mathrm{F}})$ is the density of states at Fermi level. A T_0 below 10^4 K indicates a high DOS at the Fermi level and T_0 values in the range from 1 to 10^4 K are usually found in granular metals and cermets, while amorphous semiconductors usually have T_0 above 10^4 K.

The Seebeck coefficient was measured by TETF-LN thin film thermoelectric parameter tester. The measurement has been performed on the same type of pellet samples for electrical conductivity measurements. The measurement was made in a high vacuum chamber. In the Seebeck test, the testing device is positioned across two platforms: one designated as the hot end and the other as the cold end. These ends are respectively heated by a power supply, creating a temperature difference between them. The temperature

difference ΔT at two points located in the middle of the sample is measured using a temperature meter, followed by measuring the voltage ΔV between these two points with a high-precision voltmeter. Utilizing the formula for calculating the Seebeck coefficient:

$$S = \frac{\Delta V}{\Delta T}$$

Prior to assessing the Seebeck coefficient of our sample device, we employed PEDOT as a standard reference sample to calibrate and adjust instrument parameters accordingly. The Seebeck coefficient measurements were repeated three times to get the average value and error bar.

The thermoelectric efficiency is evaluated by the dimensionless figure of merit:

$$ZT = \frac{S^2 \sigma T}{\kappa}$$

where S is Seebeck coefficient, σ is electrical conductivity, κ is thermal conductivity of materials and T is absolute temperature. Moreover, the power factor (PF) is frequently employed as a simplified parameter for assessing the thermoelectric properties of materials.

$$PF = S^2 \sigma$$

A 13 mm round pellet of Ni-BTT-OCn (thickness about 246 μm) was placed in a white thermally-insulated foam holder. The laser source is composed of a laser diode emitting at 808 nm (Thorlabs, L808P500MM) placed in a laser diode mount (Thorlabs, TCLDM9), which was controlled by a driver (TED 200C) and temperature controller (LDC 205C). The IR camera (FLIR, E30bx) was used as a temperature monitor. The laser power for each measurement was calibrated with a power sensor (Thorlabs, S310C).

The calculation of photothermal conversion efficiency was based on a previously reported method[3-5] and the details are as follows:

$$\sum_{\mathrm{i}} m_{\mathrm{i}} C_{\mathrm{p_i}} \frac{\mathrm{d}T}{\mathrm{d}t} = Q_{\mathrm{L}} - Q_{\mathrm{ext}}$$

where m_{i} and C_{pi} are the mass and heat capacity of the system components, and ΔT is the temperature difference between the sample and the surroundings. Q_{L} is the absorbed light energy and can be determined with the following equation:

$$Q_{\mathrm{L}} = I(1 - 10^{-A_{808}})\eta_{\mathrm{PT}}$$

where I is the laser power; A_{808} is the absorbance of the materials at the wavelength of 808 nm; η_{PT} is the photo-thermal conversion efficiency. Q_{ext} is the external heat lost into the

environment which is nearly proportional to the linear thermal driving force as the proportionality constant, namely:

$$Q_{\text{ext}} = hS\Delta T$$

where h is the heat transfer coefficient; S is the surface area of the system.

At the maximum steady-state temperature, $T_{\max}$, the photothermal heat energy input is equal to the external heat loss,

$$\sum_i m_i C_{p_i} \frac{dT}{dt} = Q_L - Q_{ext} = 0$$

namely,

$$Q_L = I(1 - 10^{-A_{808}})\eta_{PT} = Q_{ext} = hS\Delta T_{max}$$

and then,

$$\eta_{PT} = \frac{hS\Delta T_{max}}{I(1 - 10^{-A_{808}})}$$

In order to get hS, we focus on the cooling process, during which the laser is off and Q_L is zero, so:

$$\sum_i m_i C_{p_i} \frac{dT}{dt} = - Q_{ext} = - hS\Delta T$$

A dimensionless temperature, θ, is introduced as:

$$\theta = \frac{\Delta T}{\Delta T_{max}}$$

and we substitute it into the last equation and obtain:

$$\frac{d\theta}{dt} = - \frac{hS}{\sum_i m_i C_{p_i}} \theta$$

namely,

$$\frac{d\theta}{dt} = - \frac{hS}{\sum_i m_i C_{p_i}} d$$

whose integration formula is:

$$ln\theta = - \frac{hS}{\sum_i m_i C_{p_i}}$$

We then define:

$$\tau = - \frac{\sum_i m_i C_{p_i}}{hS}$$

Thus,

$$t = -\tau ln\theta$$

and the cooling time coefficient, τ, can be determined with a linear fit of the t-lnθ curves. Therefore:

$$hS = -\frac{\sum_i m_i C_{p_i}}{\tau}$$

and then:

$$\eta_{PT} = \frac{hS\Delta T_{max}}{I(1-10^{-A_{808}})} = \frac{\sum_i m_i C_{p_i}\Delta T_{max}}{\tau I(1-10^{-A_{808}})} \geq \frac{mC_p\Delta T_{max}}{\tau I(1-10^{-A_{808}})}$$

where I is the laser power; A_{808} is the absorbance of the materials at a wavelength of 808 nm; h is the heat transfer coefficient; S is the surface area of the system; m_i and C_{pi} are the mass and heat capacity of the system components, respectively; τ is the cooling time coefficient; ΔT_{max} is the temperature difference between the maximum and the ambient temperature.

The solubility of Ni-BTT-OCn in solvents was determined as follows. The solvent was added by portions (20, 10 or 5 μL each time) into a small bottle with ~1 mg of sample for each Ni-BTT-OCn at room temperature (RT). The mixture was gently stirred for 5 min after adding the solvent each time. The Ni-BTT-OCn was regarded as dissolving completely until no particle can be seen on bottle wall after swing. Then the solubility of the Ni-BTT-OCn was obtained based on the mass of the sample and the total volume of solvent.

The contact angle tests were performed on a Dataphysics SDC-350KS Micro surface contact angle analyzer. The surface energy of the polymers was characterized and calculated by the contact angles of the two probe liquids with the Owens-Wendt equation:

$$(1+\cos\theta)\gamma_{pl} = 2\left(\gamma_s{}^d\gamma_{spl}{}^d\right)^{1/2} + 2\left(\gamma_s{}^p\gamma_{spl}{}^p\right)^{1/2}$$

where γ_s and γ_{pl} are the surface energy of the sample and the probe liquid, respectively. The superscripts d and p refer to the dispersion and polar components of the surface energy, respectively.[6]

Synthetic Procedures

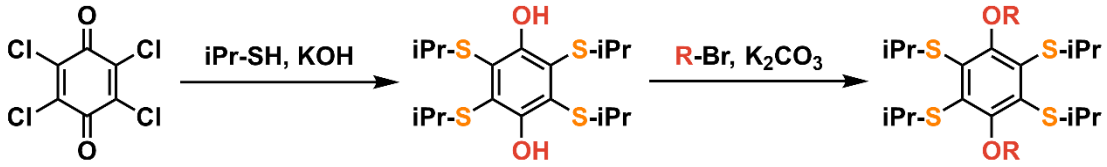

Taking poly(nickel-3,6-dihexyloxybenzene-1,2,4,5-tetrakis(thiolate)) (Ni-BTT-OC6) as an example, the synthesis method is elaborated in detail.[7] Potassium hydroxide (7.57 g, 135 mmol) and isopropyl mercaptan (18.1 mL, 195 mmol) were added to 70 mL of toluene, under argon protection, stirring at room temperature for 2 h. Then the toluene solution containing 7.38 g (30 mmol) of 2,3,5,6-tetrachlorobenzoquinone was transferred into the system drop by drop, under argon protection, and reacted at 60 °C for 15 ~ 21 h. After the reaction, the mixture was cooled to room temperature, 100 mL of deionized water was added to wash the reaction solution, then the aqueous phase was extracted with dichloromethane, the organic phases were combined and dried with anhydrous magnesium sulfate, and the residue was recrystallized with methanol after the organic solvents were removed under reduced pressure to obtain 2,3,5,6-tetraisopropylthio-1,4-benzenediol. 4.88 g (12 mmol) of the intermediate and 9.95 g (72 mmol) of potassium carbonate were added to 100 mL of DMF and 100 mL of toluene as a mixed solvent, 4.75 g (28.8 mmol) of 1-bromohexane was added under argon protection, and the reaction was carried out under argon protection and 100 °C for 15 ~ 24 h. At the end of the reaction, the reaction was cooled to room temperature, 100 mL of deionized water was added to wash the reaction solution, and then the aqueous phase was extracted with dichloromethane, the organic phases were combined and dried with anhydrous magnesium sulfate, and the residue was purified by column chromatography after the organic solvent was removed under reduced pressure to obtain 1,4-dihexyloxy-2,3,5,6-tetrakis(isopropylthio)benzene (BTT-OC_6H_{13}) (5.93 g, 10 mmol, 86%). ^{1}H NMR ($CDCl_3$, δ): 3.97 (t, 4H, –OCH_2), 3.83 (sep, 4H, CH), 1.79 (m, 4H, O–CH_2–CH_2), 1.50 (m, 4H, O–CH_2–CH_2–CH_2), 1.36 (overlapping, m, 16H), 1.19 (d, 24H), 0.91 (t, 6H). ^{13}C NMR ($CDCl_3$): 157.75, 134.59, 72.48, 38.44, 38.43, 31.67, 30.36, 25.71, 22.94, 22.62, 14.01.

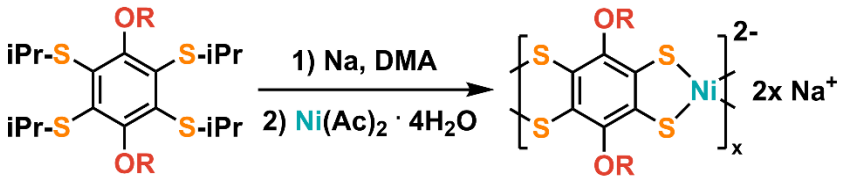

BTT-OC_6H_{13} (0.288 g, 0.50 mmol) was dissolved in anhydrous N,N-dimethylacetamide (80 mL). Sodium (1.15 g, 50 mmol) was added to the solution and the mixture heated to 100 °C for 24 h, during which a milky orange slurry formed. 20 mL of thoroughly degassed water was added to obtain clear orange-brown solution. Nickel acetate tetrahydrate ($NiAc_2 \cdot 4H_2O$, 0.117 g, 0.47 mmol) was dissolved in 20 mL of degassed water and added dropwise to the reaction mixture over 20 min. Over the course of the Ni addition, the color of the reaction mixture gradually deepened to black. After complete addition, the mixture was heated to 100 °C for 24 h. The reaction was cooled to room temperature and the black solid collected by centrifugation. The crude product was purified by washing five times with deionized water, methanol, and ether to remove low molecular weight oligomers and ionic impurities. The purified polymer was dried under vacuum at 100 °C for 24 h, and the black powder was recovered as Ni-BTT-OC6 (0.128 g, 0.28 mmol, 56%).[8]

Poly(nickel-3,6-di(dodecyloxy)benzene-1,2,4,5-tetrakis(thiolate)) (Ni-BTT-OC12) and poly(nickel-3,6-di(octadecyloxy)benzene-1,2,4,5-tetrakis(thiolate)) (Ni-BTT-OC18) were synthesized by the same method, with yields of 67% and 55%, respectively.

Compositional and Structural Characterization

Due to the insufficient solubility of the three Ni-BTT-OCn polymers in all common solvents compatible with gel permeation chromatography (GPC), reliable molecular weight distributions could not be obtained by conventional GPC. This insolubility is a well-recognized challenge in the characterization of rigid coordination polymers. Nevertheless, the combined results from EA, TGA, UV-vis-NIR, and PXRD spectra confirm that the obtained products are polymers rather than oligomers.

Tab. S1 Experimental and theoretical elemental analysis of Ni-BTT-OCn.

Sample	**Chemical Formula**	**C (wt%)**	**H (wt%)**	**S (wt%)**	**O (wt%)**	**Ni (wt%)**
C6	$Ni(C_{18}H_{26}S_4O_2)(DMAc)(H_2O)$	47.64	6.28	22.3	13.6	10.54
		Atomic Ratio				
		Found	Ni : C : H : S : O = 1 : 22.1 : 34.9 : 3.8 : 4.7			
		Theoretical	Ni : C : H : S : O = 1 : 22.0 : 37.0 : 4.0 : 4.0			
C12	$Ni(C_{30}H_{50}S_4O_2)_{0.9}(DMAc)_{0.2}(H_2O)_2$	52.62	7.22	16.97	10.56	8.94
		Atomic Ratio				
		Found	Ni : C : H : S : O = 1 : 28.9 : 47.7 : 3.5 : 4.4			
		Theoretical	Ni : C : H : S : O = 1 : 27.8 : 50.8 : 3.6 : 4.0			
C18	$Ni(C_{42}H_{74}S_4O_2)_{0.8}(DMAc)(H_2O)_3$	57.27	7.79	11.86	11.09	7.04
		Atomic Ratio				
		Found	Ni : C : H : S : O = 1 : 33.6 : 65.3 : 3.1 : 5.7			
		Theoretical	Ni : C : H : S : O = 1 : 39.3 : 72.2 : 3.2 : 5.6			

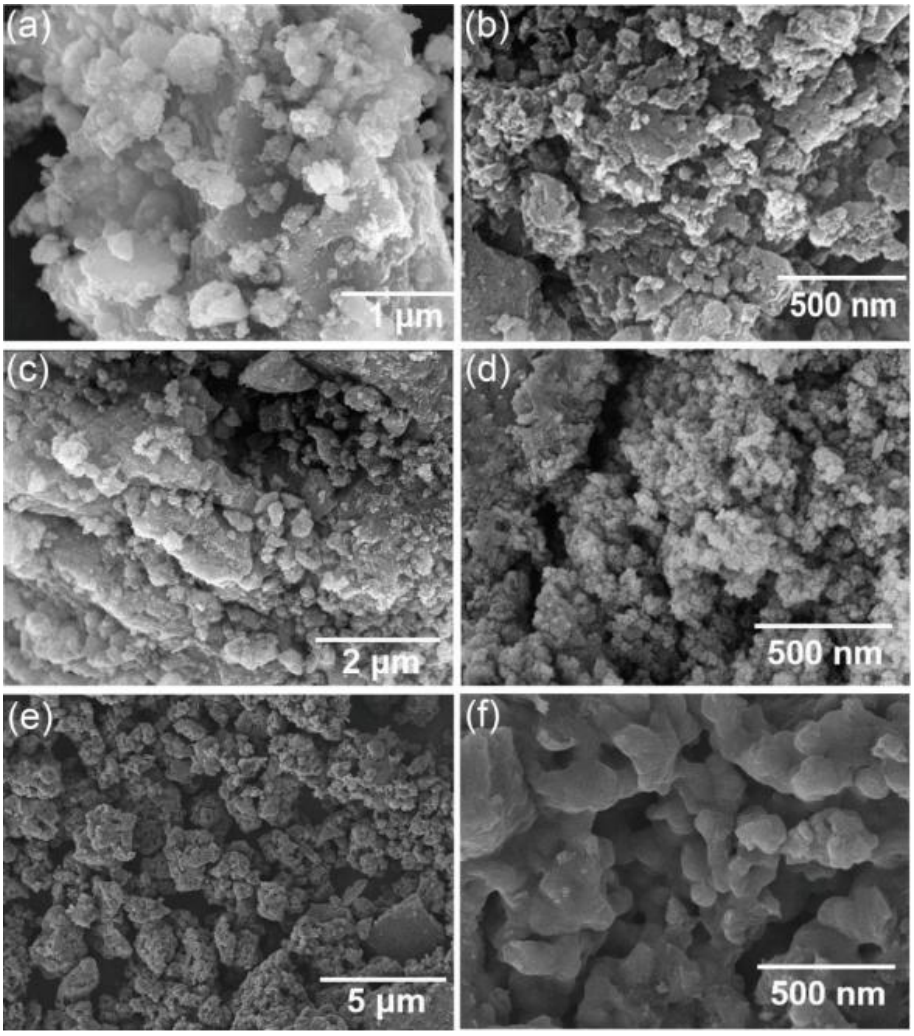

Fig. S1 SEM images of as-prepared (a, b) Ni-BTT-OC6, (c, d) Ni-BTT-OC12, and (e, f) Ni-BTT-OC18 powder.

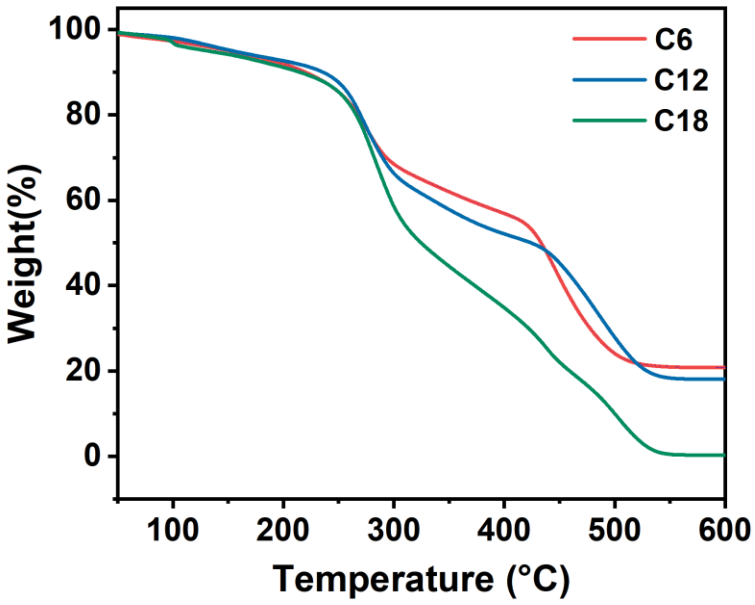

Fig. S2 TGA spectra recorded in nitrogen.

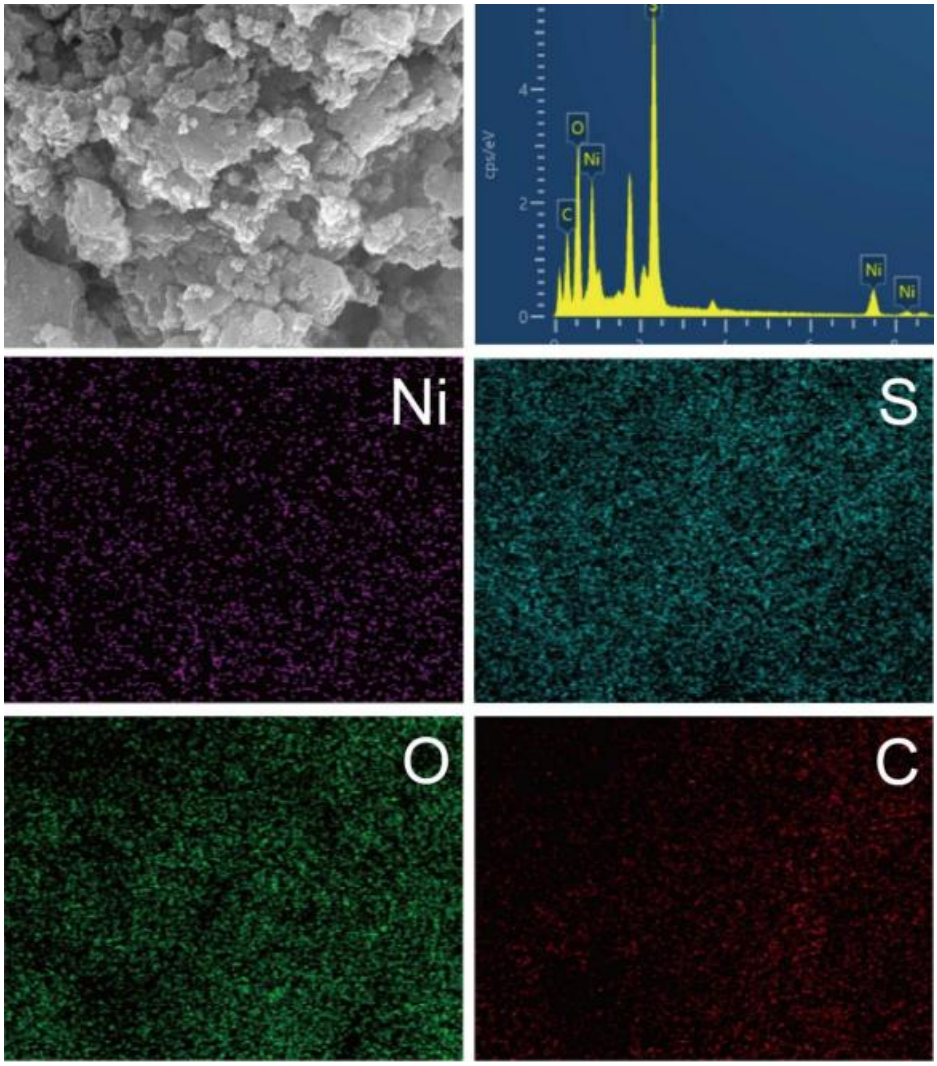

Fig. S3 SEM image (top left) and EDS spectrum (top right) of compressed Ni-BTT-OC6 pellets. Bottom row: element distribution maps of nickel (Ni), sulfur (S), oxygen (O), and carbon (C) for the compressed pellets.

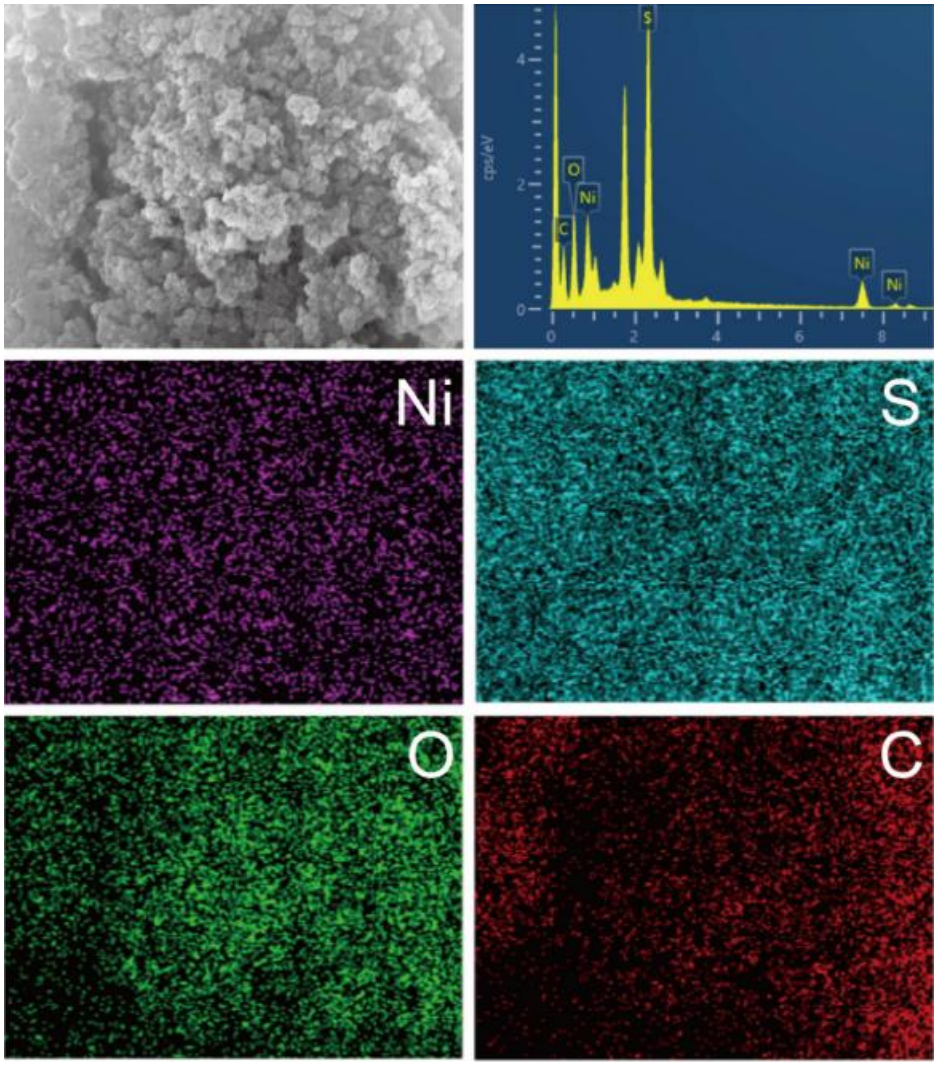

Fig. S4 SEM image (top left) and EDS spectrum (top right) of compressed Ni-BTT-OC12 pellets. Bottom row: element distribution maps of nickel (Ni), sulfur (S), oxygen (O), and carbon (C) for the compressed pellets.

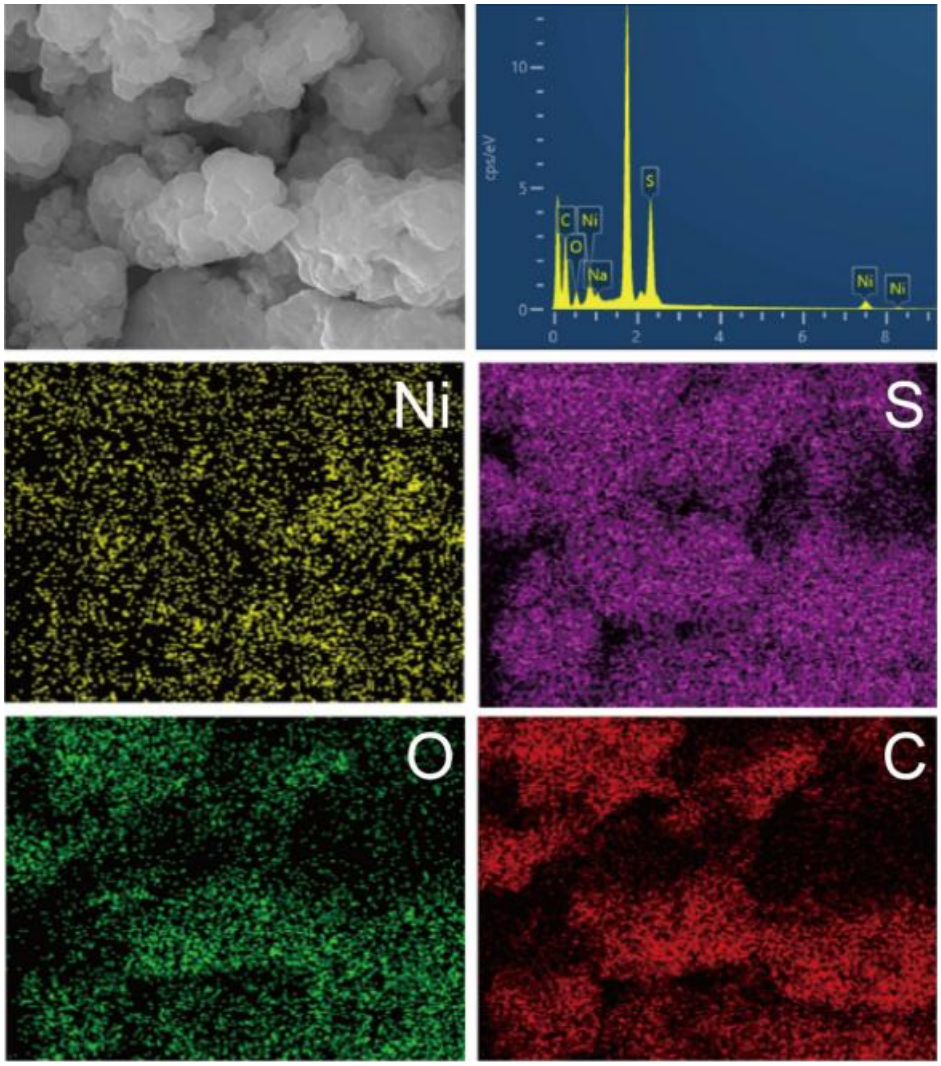

Fig. S5 SEM image (top left) and EDS spectrum (top right) of compressed Ni-BTT-OC18 pellets. Bottom row: element distribution maps of nickel (Ni), sulfur (S), oxygen (O), and carbon (C) for the compressed pellets.

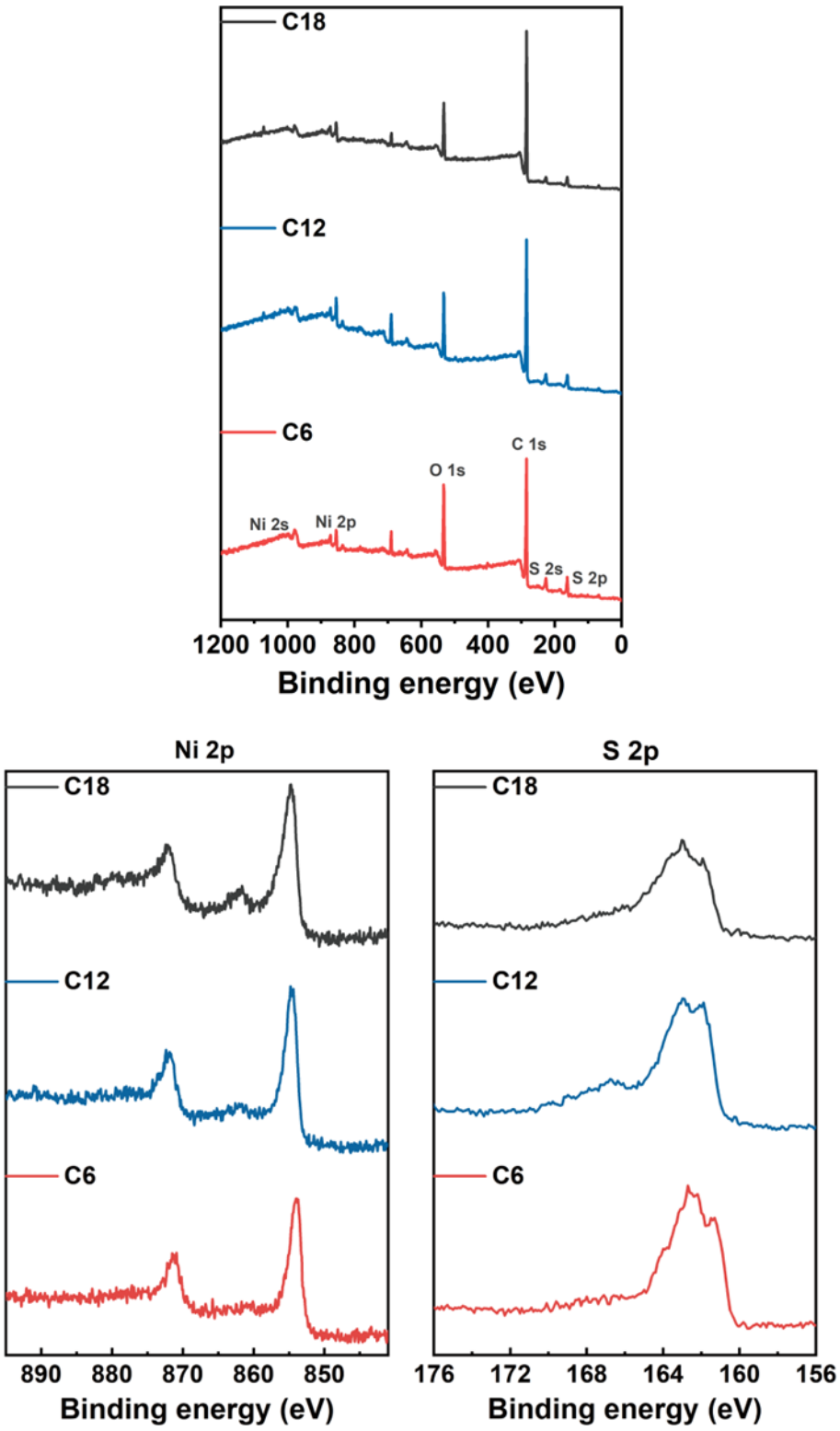

Fig. S6 XPS spectra of Ni-BTT-OCn.

Tab. S2 FT-IR peak assignments for Ni-BTT-OCn.

Wavenumber (cm^{-1})	Assignment	Significance
~1160, ~1000	C=S· stretching	Confirms the radical character of the polymer backbone, consistent with prior Ni-BTT reports[8]
~1248	C–O (Ar–O–R) stretching	Confirms successful integration of alkoxy side chains into the coordination polymer backbone
~1600, ~1498	Aromatic C=C stretching	Benzene ring skeleton vibration
~2955, ~2925, ~2850	C–H stretching	$–CH_2–$, $–CH_3$ asymmetric/symmetric stretching

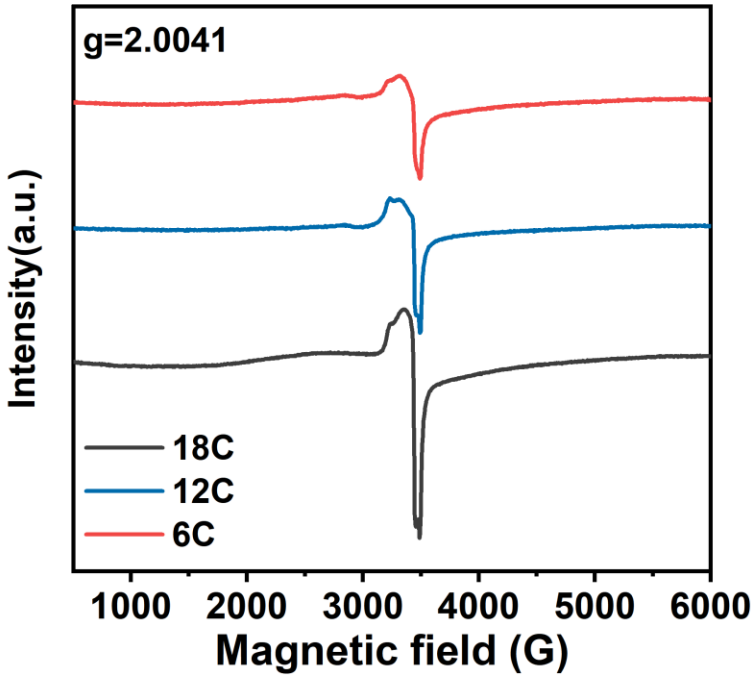

Fig. S7 EPR spectra of Ni-BTT-OCn.

Tab. S3 EXAFS fit parameters for Ni-BTT-OCn.

Sample	N [a]	R [b] (Å)	σ^2 [c] (Å^2)	R Factor [d]
Ni-BTT-OC6	3.3(5)	2.32(2)	0.0073	0.015
Ni-BTT-OC12	3.8(4)	2.15(1)	0.0032	0.013
Ni-BTT-OC18	2.9(3)	2.13(1)	0.0012	0.021

[a] N, coordination number; [b] R, the distance between absorber and backscatter atoms; [c] σ^2, the Debye Waller factor value; [d] R factor indicates the goodness of the fit. Fitting conditions: k range: 3-12; R range: 1-3; fitting space: R space; k weight =1, 2. A reasonable range of EXAFS fitting parameters: $0.700 < S_0^2 < 1.000$; $CN > 0$; $\sigma^2 > 0$ Å^2; $|\Delta E_0| < 15$ eV; R factor < 0.025.

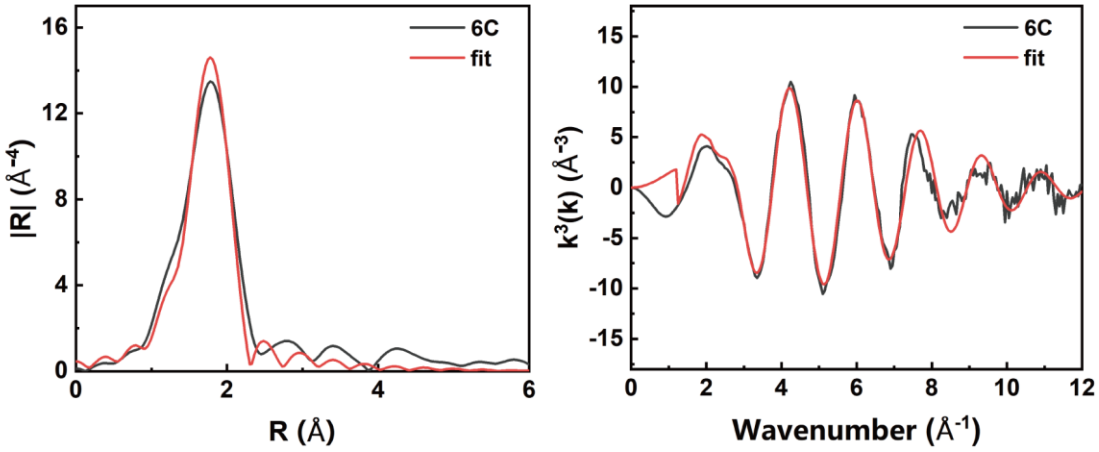

Fig. S8 EXAFS spectra in R-space (left) and k-space (right) of Ni K-edge absorption of Ni-BTT-OC6.

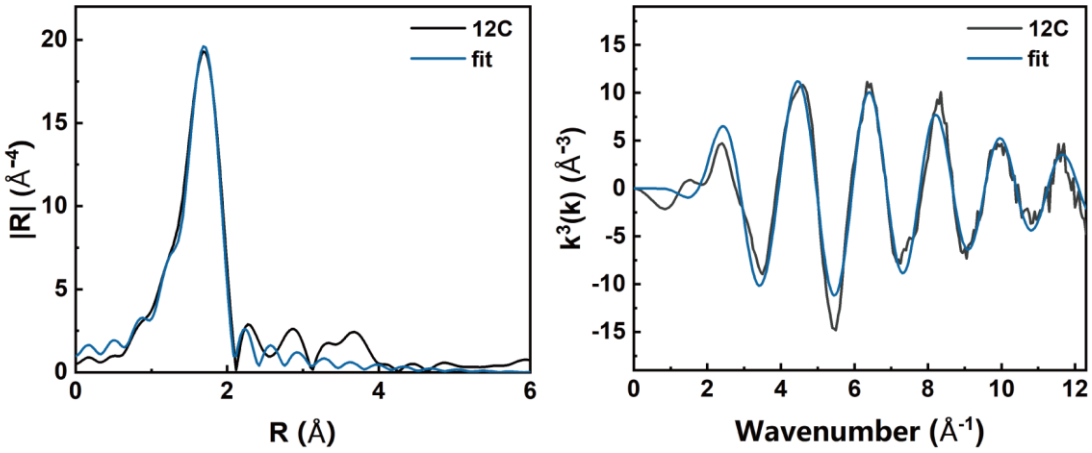

Fig. S9 EXAFS spectra in R-space (left) and k-space (right) of Ni K-edge absorption of Ni-BTT-OC12.

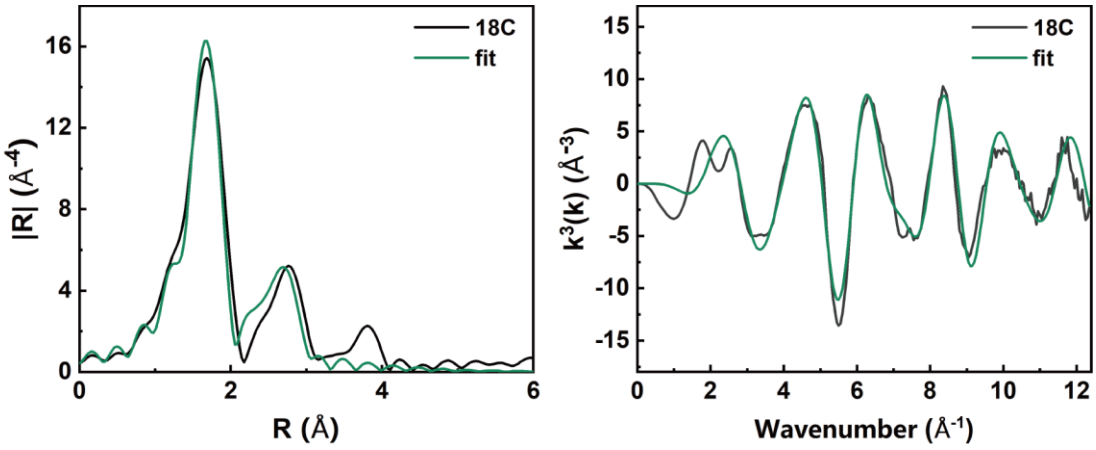

Fig. S10 EXAFS spectra in R-space (left) and k-space (right) of Ni K-edge absorption of Ni-BTT-OC18.

Physical Characterization

Tab. S4 Summary of physical properties for Ni-BTT-OCn.

Physical properties	Ni-BTT-OC6	Ni-BTT-OC12	Ni-BTT-OC18
Electrical conductivity (S cm^{-1})	0.56(1)	0.033(9)	0.012(2)
Seebeck coefficient (μV K^{-1})	32.7(6)	44.7(1)	69.2(1)
PF (μW m^{-1} K^{-2})	$6.0(2)\times10^{-2}$	$6.6(2)\times10^{-3}$	$5.9(1)\times10^{-3}$
Arrhenius fit, E_a (eV)	0.0956	0.208	0.327
Mott 3D VRH fit, T_0 (K)	1.2×10^7	2.8×10^8	1.7×10^9
Work function, Φ (eV)	3.17	3.27	3.84
Band gap (eV)	0.60	0.74	0.85

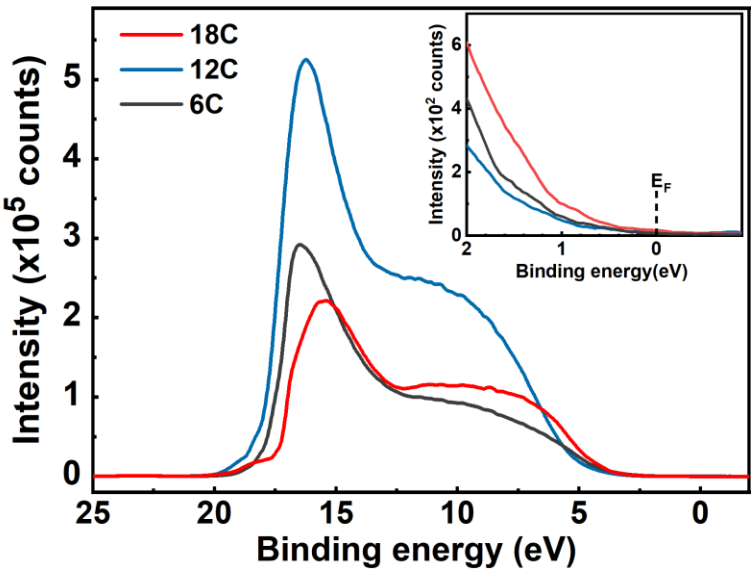

Fig. S11 UPS valence band spectra of Ni-BTT-OCn. The enlarged Fermi edge energy region is shown in the inset.

NIR Photothermal Conversion

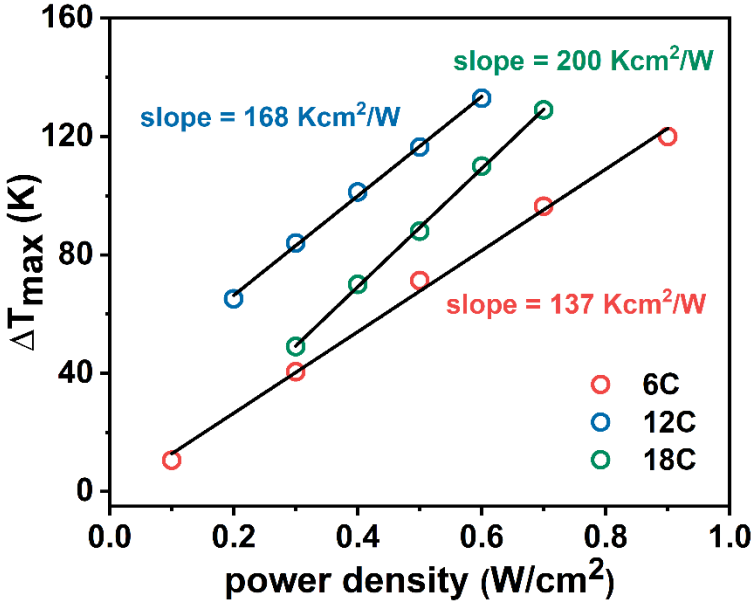

Fig. S12 Linear relationships between temperature and irradiation power densities.

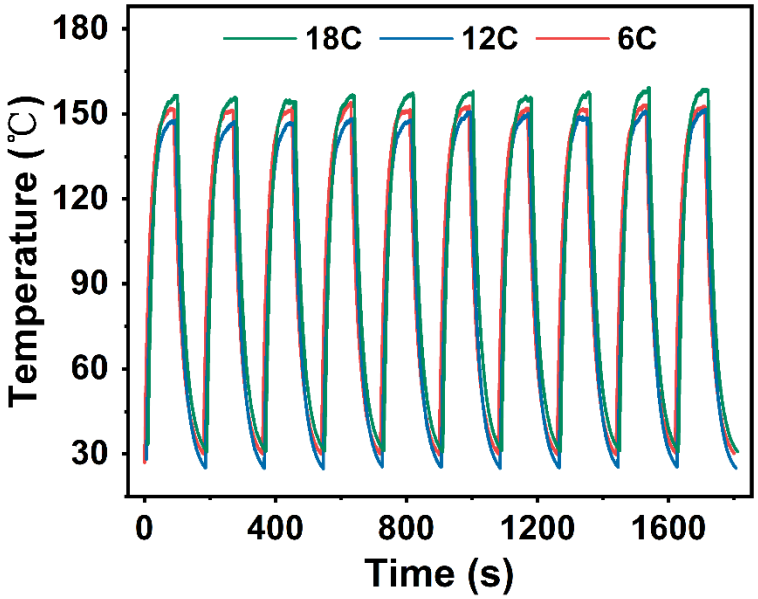

Fig. S13 Reproducibility tests on Ni-BTT-OCn pellets at 0.9 W cm^{-2}, 0.7 W cm^{-2}, and 0.7 W cm^{-2}, respectively (10 heating-cooling cycles).

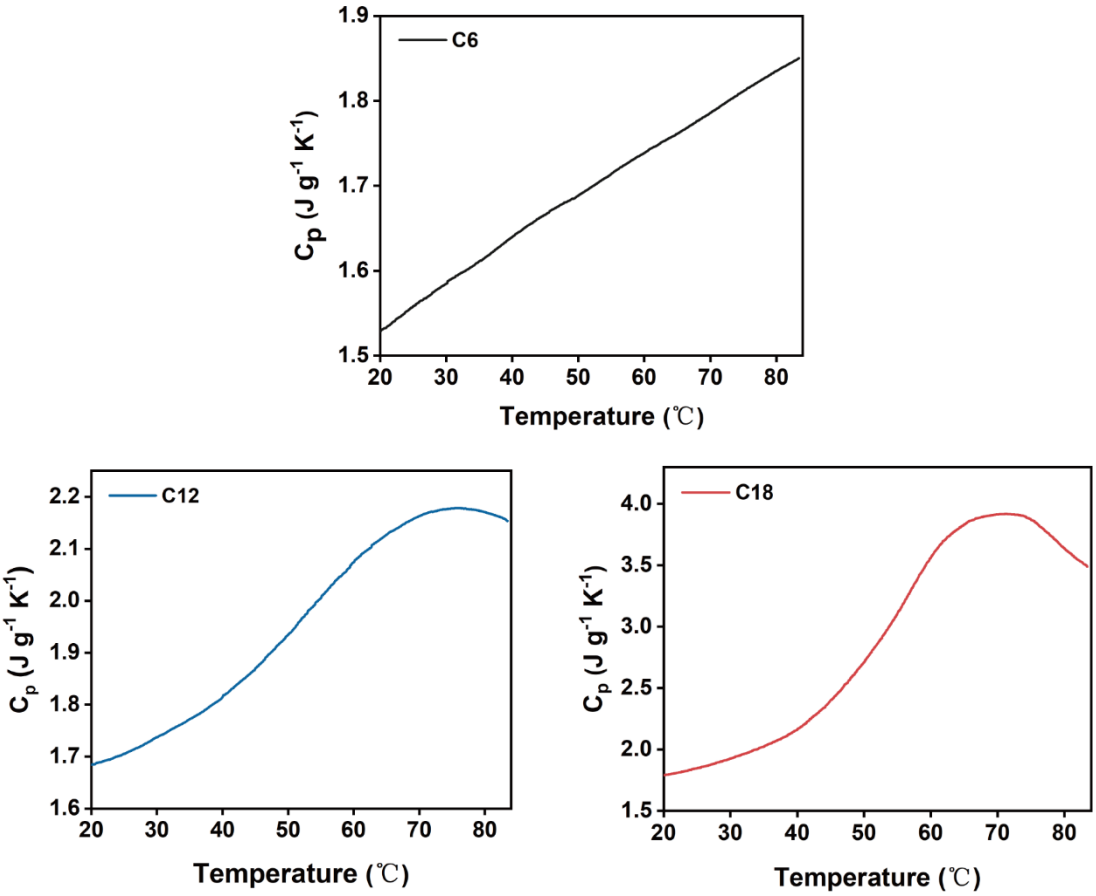

Fig. S14 Temperature-dependent heat capacity C_p over 20 ~ 110 ℃ of Ni-BTT-OCn.

Tab. S5 Parameters for PT efficiency calculation.

Sample	m (mg)	C_p (J g^{-1} K^{-1})	τ (s)	S_{spot} (cm^2)	K (K cm^2 W^{-1})	$\Delta T/I$ (K W^{-1})	$1\text{-}10^{-A808}$	η_{PT} (%)
C6	70	1.59	22.6	1.3	137	105	0.97	54
C12	70	1.74	27.6	1.3	168	129	0.98	58
C18	72	1.94	36.4	1.3	200	154	0.97	61

Tab. S6 Comparison of properties of Ni-BTT-OCn and other PT materials.

Compound	S (μV K^{-1})	η_{PT} (%)	Ref
C6	32.03	54	
C12	45.78	58	This work
C18	70.07	61	
PEDOS-C6	103	42.5	[3]
NiTTFtt	-3.6	71	[9]
Li-NiTTFtt	10.0	94	[9]
$TaTe_2$	7.1	30.2	[10]
NiV_{14}	6380	16.04	[11]
MoS_2/Carbon	1080	39.6	[12]
CWO@PU	2870	42.7	[13]

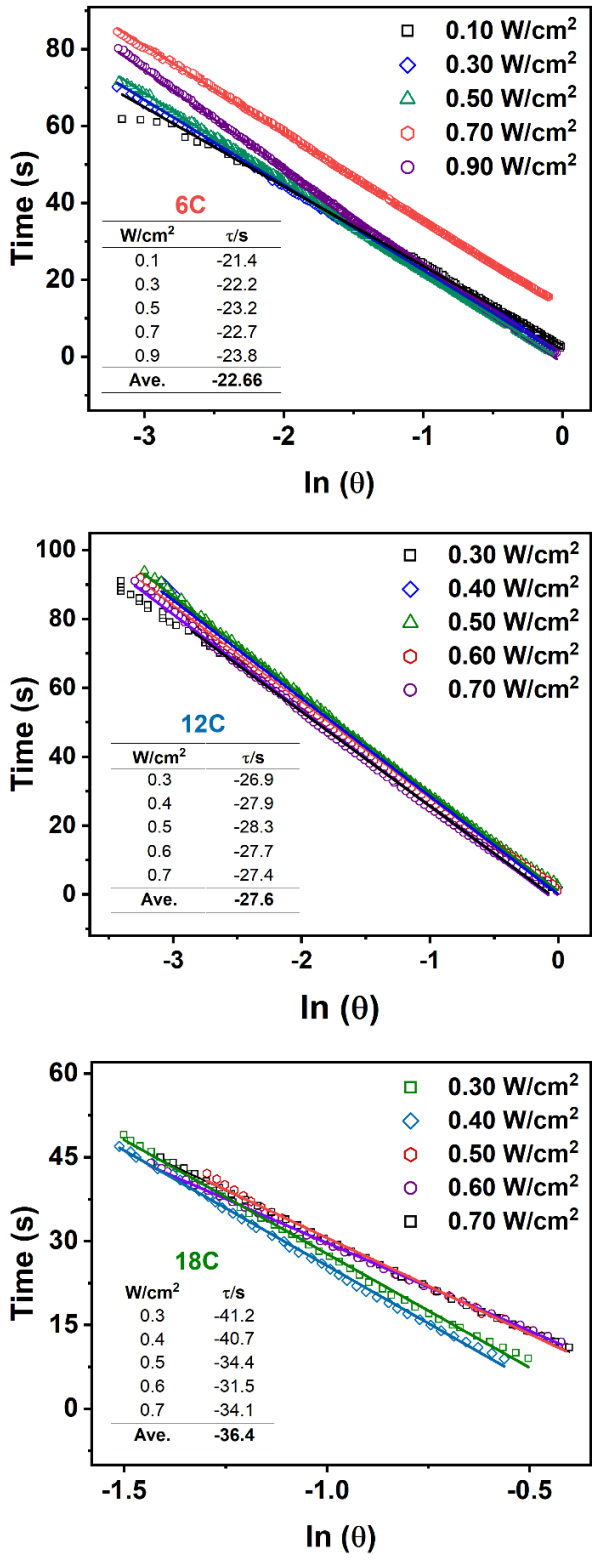

Fig. S15 The time-lnθ linear curves corresponding to the cooling process (laser off) of Ni-BTT-OCn.

Solubility

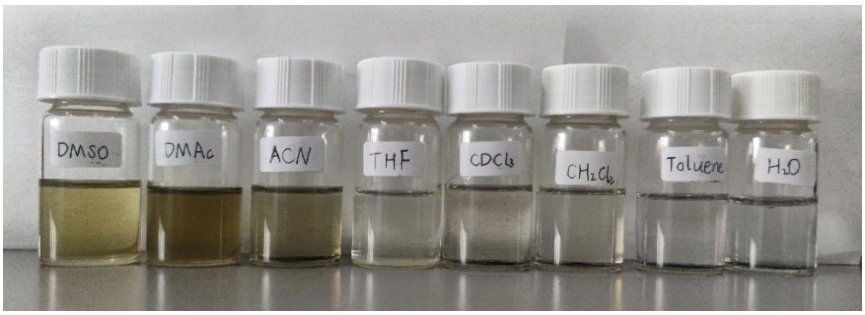

Fig. S16 Solubility measurements of Ni-BTT-OC6 in common solvents.

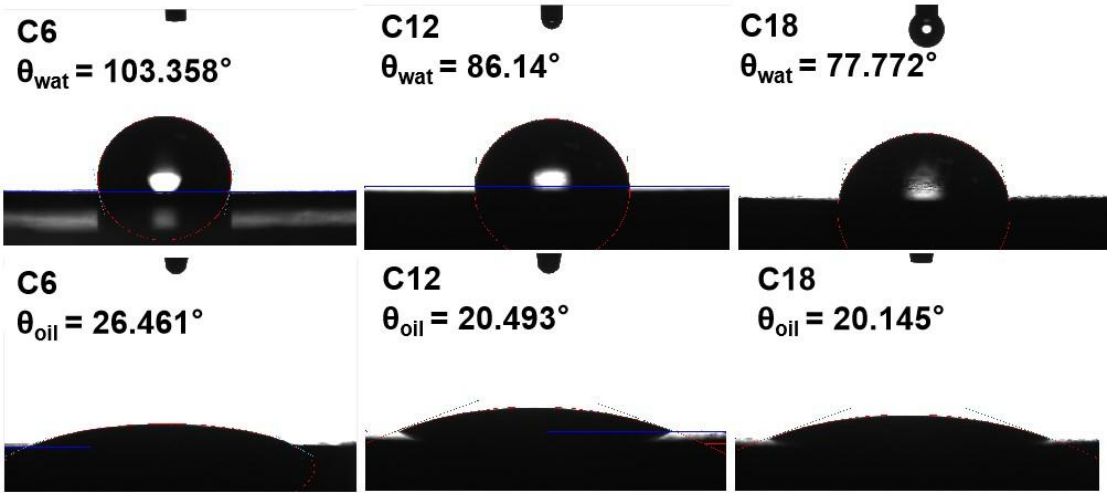

Fig. S17 Contact angles of water and n-hexadecan for Ni-BTT-OCn.

Tab. S7 The contact angles and surface energy parameters of Ni-BTT-OCn.

Sample	θ_{wat} (°)	θ_{oil} [a] (°)	γ_d [b] (mN m^{-1})	γ_p [b] (mN m^{-1})	γ (mN m^{-1})
C6	103.4	26.46	24.78	0.44	25.22
C12	86.1	20.49	25.88	4.47	30.35
C18	77.8	20.15	25.94	8.11	34.05

[a] θ_{oil} represents the contact angle of n-hexadecane.

[b] γ_d and γ_p represent the surface free energies generated from the dispersion forces and the polar forces, respectively.

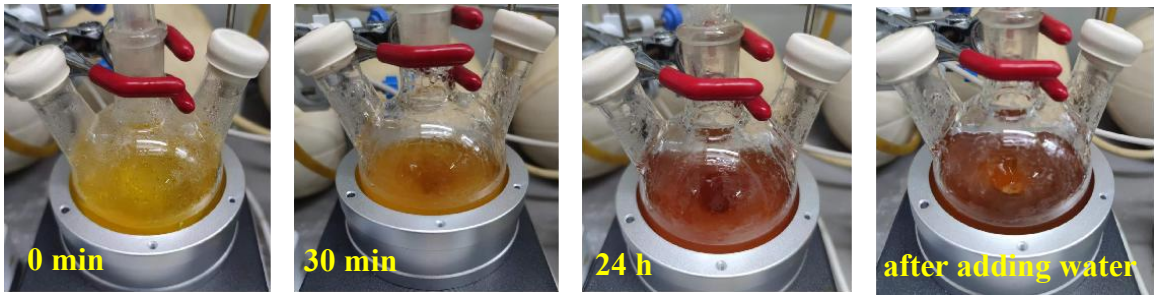

Fig. S18 Photographs showing the color change of the reaction mixture during the synthesis of monomeric sodium tetrasulfide intermediate under nitrogen atmosphere.

NMR Characterization of Organic Ligands

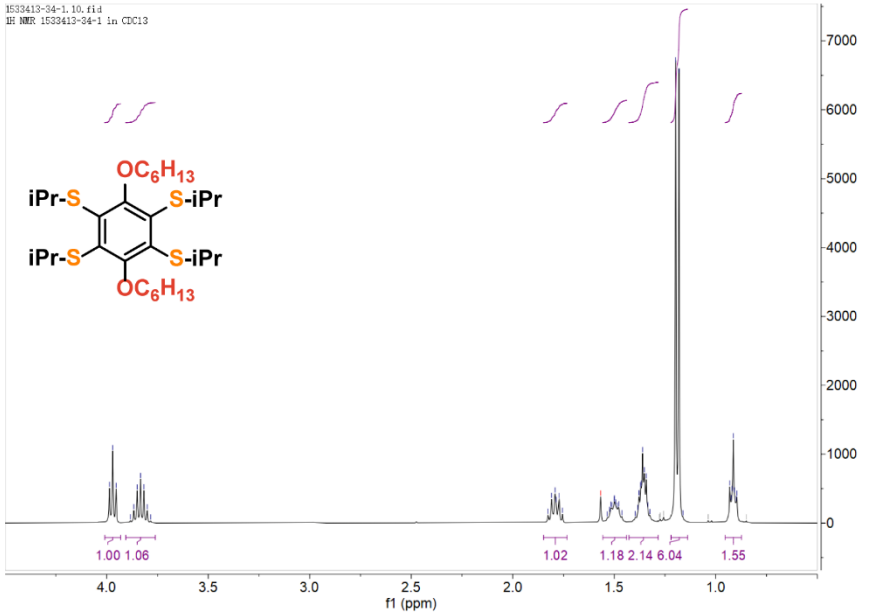

Fig. S19 ^{1}H NMR of BTT-OC_6H_{13}.

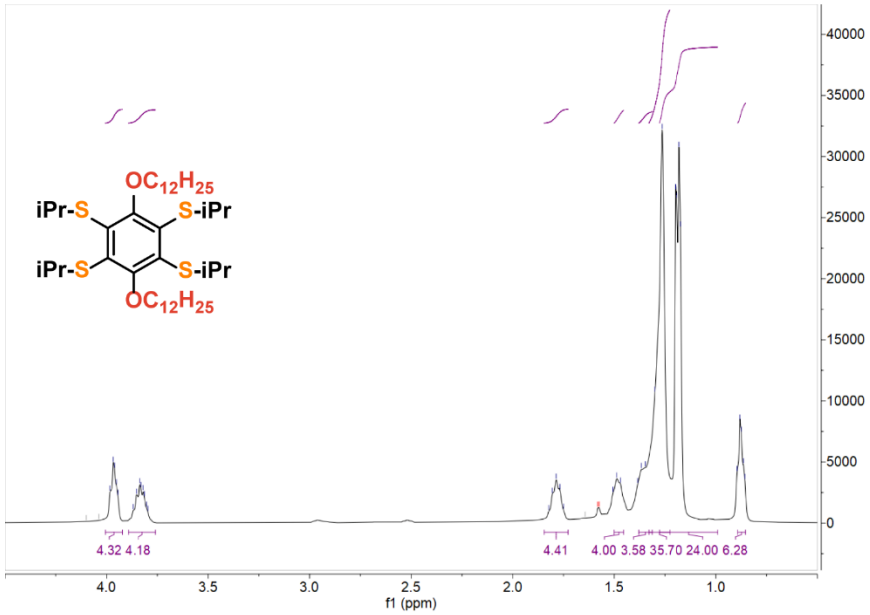

Fig. S20 ^{1}H NMR of BTT-$OC_{12}H_{25}$.

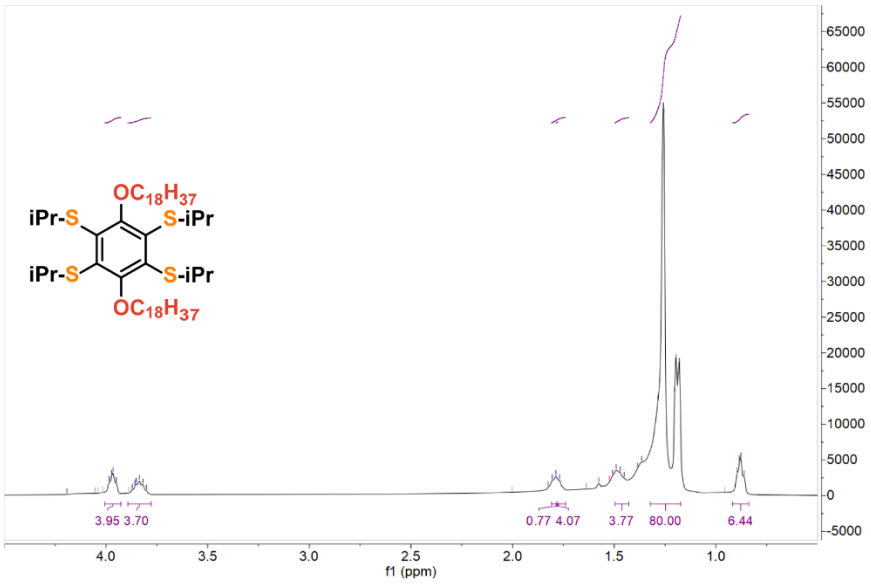

Fig. S21 ^{1}H NMR of BTT-$OC_{18}H_{37}$.

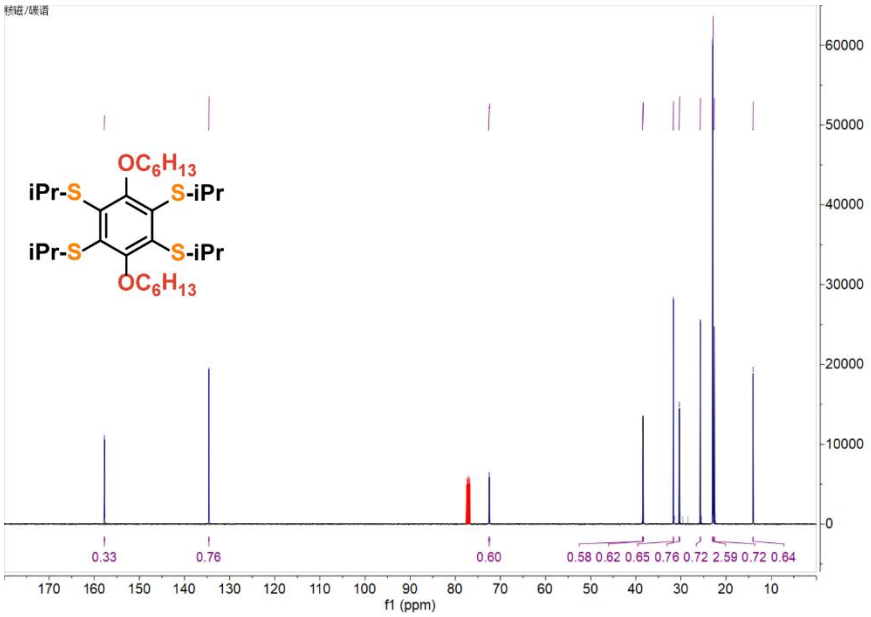

Fig. S22 ^{13}C NMR of BTT-OC_6H_{13}.

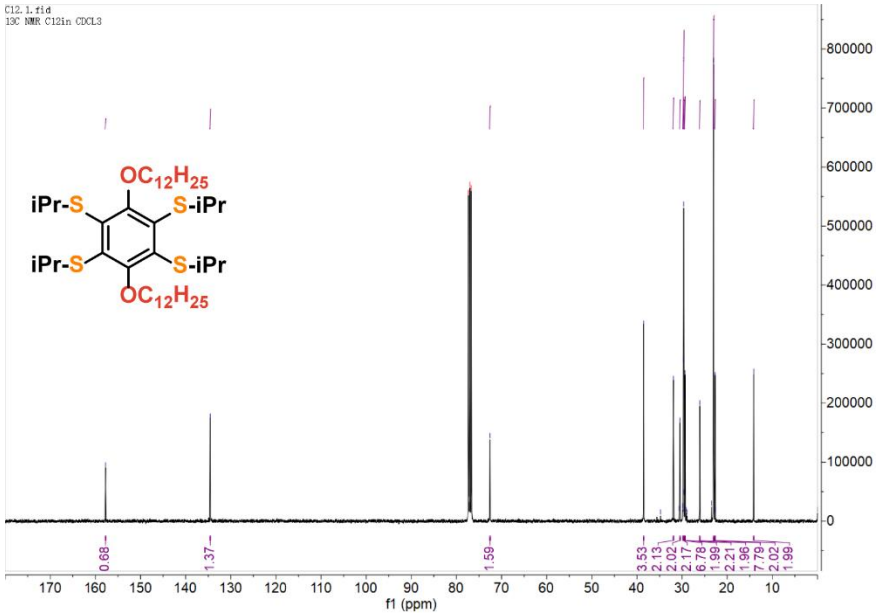

Fig. S23 ^{13}C NMR of BTT-$OC_{12}H_{25}$.

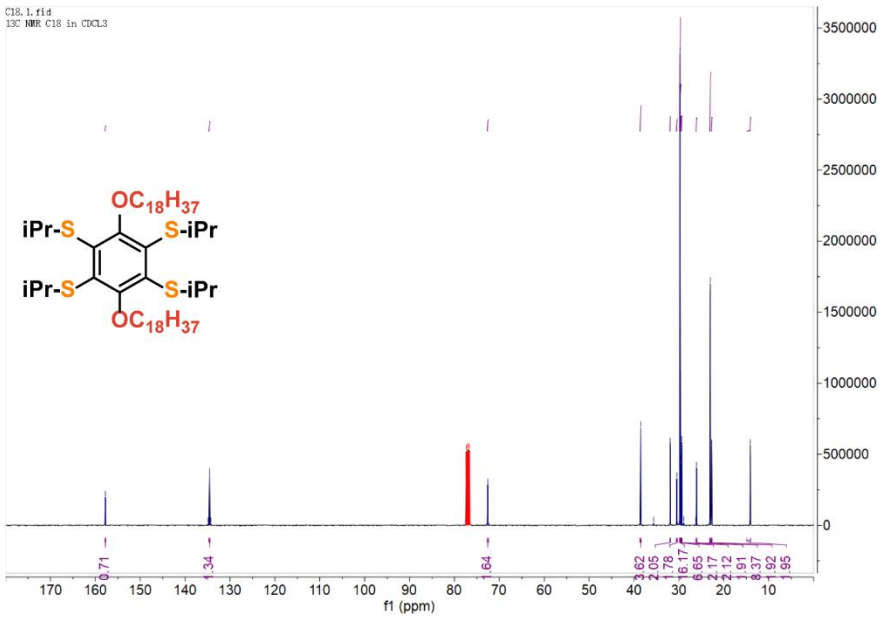

Fig. S24 ^{13}C NMR of BTT-$OC_{18}H_{37}$.

References

1. B. Ravel and M. Newville, *J. Synchrot. Radiat*., 2005, **12**, 537-541.

2. S. I. Zabinsky, J. J. Rehr, A. Ankudinov, R. C. Albers and M. J. Eller, *Phys. Rev. B*, 1995, **52**, 2995-3009.

3. B. Kim, H. Shin, T. Park, H. Lim and E. Kim, *Adv. Mater.*, 2013, **25**, 5483-5489.

4. Y. Wang, W. G. Zhu, W. N. Du, X. F. Liu, X. T. Zhang, H. L. Dong and W. P. Hu, *Angew. Chem. -Int. Edit.*, 2018, **57**, 3963-3967.

5. A. Pasciak, A. Pilch-Wróbel, L. Marciniak, P. J. Schuck and A. Bednarkiewicz, *ACS Appl. Mater. Interfaces*, 2021, **13**, 44556-44567.

6. D. K. Owens and R. C. Wendt, *J. Appl. Polym. Sci.*, 1969, **13**, 1741-1747.

7. Z. Wang, B. Liu and W. Qiao, **CN103483391B**, 2016.

8. Z. L. Liu, T. J. Liu, C. N. Savory, J. P. Jurado, J. S. Reparaz, J. W. Li, L. Pan, C. F. J. Faul, I. P. Parkin, G. Sankar, S. Matsuishi, M. Campoy-Quiles, D. O. Scanlon, M. A. Zwijnenburg, O. Fenwick and B. C. Schroeder, *Adv. Funct. Mater.*, 2020, **30,** 2003106.

9. J. Xie, J.-A. Pan, B. Cheng, T. Ma, A. S. Filatov, S. N. Patel, J. Park, D. V. Talapin and J. S. Anderson, *J. Am. Chem. Soc.*, 2022, **144**, 19026-19037.

10. C. Xia, T. Yu, J. Y. Liu, X. Li, J. J. Wang, S. H. Ma, G. S. Yang, H. L. Qiu, Z. G. Hu, N. Ye, J. Y. Wang and Y. C. Wu, *Adv. Opt. Mater.*, 2024, **12**, 2400314.

11. Y. Wang, C. Liu, Y. Wang, C. Zhu, X. Chen and B. Liu, *ChemSusChem*, 2021, **14**, 5434-5441.

12. Y. B. Xue, H. T. Jiang, P. Luo, H. J. Liu, Y. H. Yang, Q. K. Xue, B. Wu, G. L. Zhang, M. Zheng, M. Zheng, Z. S. Wang and M. P. Zhuo, *Adv. Funct. Mater.*, 2025, **35**, 2422592.

13. S. Zhuo, W. Jiang, Y. Dong Zhao, J.-Z. Liu, X. Zhao, J. Ye, M. Zheng, Z.-S. Wang, X.-Q. Zhou, X.-Q. Wang, Y.-L. Shi, W. Chen, K.-Q. Zhang, L.-S. Liao and M.-P. Zhuo, *Chem. Eng. J.*, 2024, **479**, 147571.